

Electronic Supplementary Information

Oxazine: an anchoring group serving as functional kernels to construct single-molecule switches

Shi Li,^a Yuxuan Jiang,^{a,b} Yudi Wang,^a Dongying Lin,^a Haoyang Pan,^{a,c}
Yongfeng Wang,^a Stefano Sanvito,^d and Shimin Hou*^{a,b}

a. Key Laboratory for the Physics and Chemistry of Nanodevices, School of Electronics, Peking University, Beijing 100871, China

b. Centre for Nanoscale Science and Technology, Academy for Advanced Interdisciplinary Studies, Peking University, Beijing 100871, China.

c. Institute of Spin Science and Technology, South China University of Technology, Guangzhou 511442, China

d. School of Physics, AMBER and CRANN Institute, Trinity College, Dublin 2, Ireland

Section 1: Phonon spectrum calculations on molecular junctions constructed with oxazine anchors and SWCNT electrodes

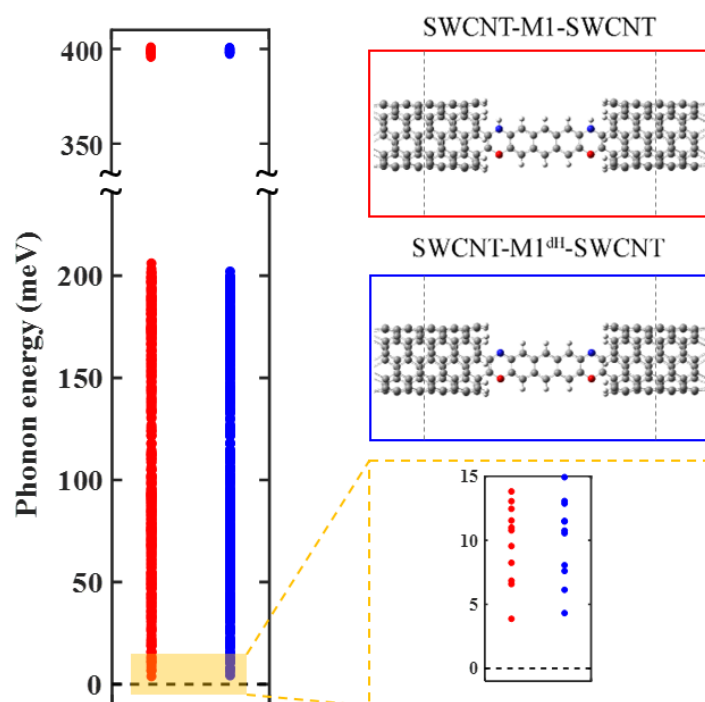


Figure S1 Vibrational frequencies calculated for the SWCNT-M1-SWCNT (red) and SWCNT-M1^{dH}-SWCNT (blue) junctions with the dynamic regions denoted by the grey dotted lines.

The phonon spectra of the junctions are computed by using the frozen phonon method,¹ in which the force constant matrix is calculated by displacing each atom in the dynamic region along the Cartesian directions with a displacement of ± 0.02 Å and by calculating the resulting forces acting on the atoms.

The phonon spectra of the SWCNT-M1-SWCNT and SWCNT-M1^{dH}-SWCNT junctions are shown in Figure S1. As we can see, there are no imaginary frequencies in the low-frequency region, indicating that these two junction structures are at least at a local minimum. The much higher frequencies around 400 meV are assigned to the stretching modes of the N-H and/or C-H bonds due to the much smaller mass of the hydrogen atoms. These results demonstrate the junction structures constructed via the oxazine anchors are dynamically stable with SWCNT electrodes.

Section 2: Molecular dynamics simulations on molecular junctions constructed with oxazine anchors and SWCNT electrodes

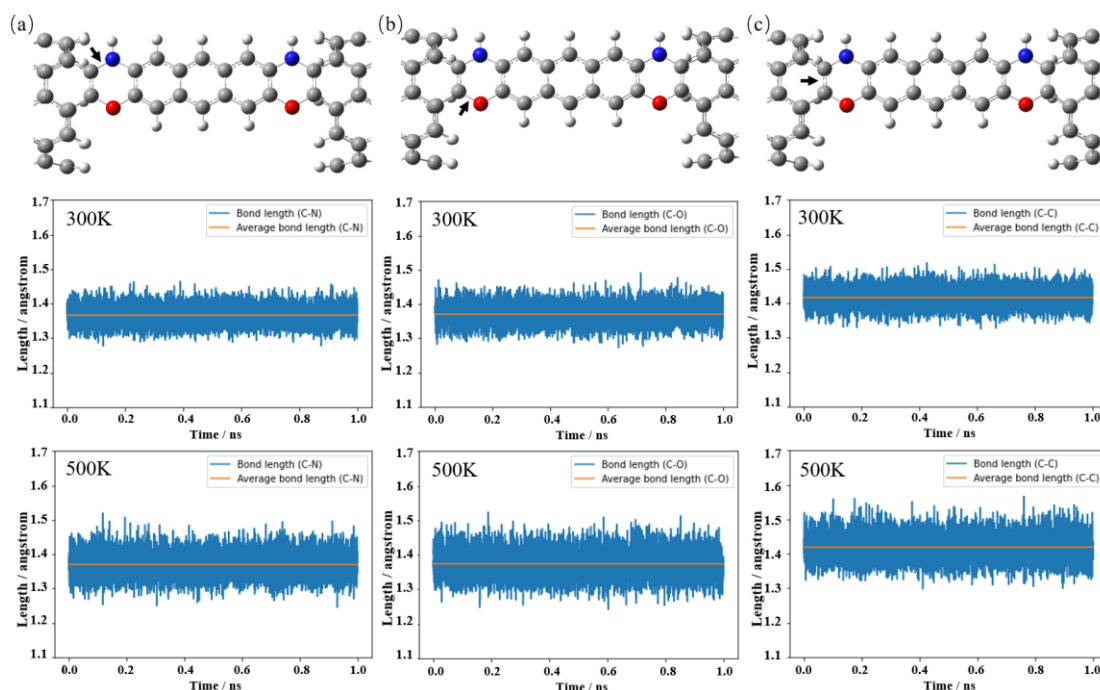


Figure S2 Variation in the C-N (a), C-O (b) and C-C (c) bond lengths marked by black arrows (the upper panel) in the SWCNT-M1-SWCNT junction obtained from MD simulations performed at 300 K (the middle panel) and 500 K (the bottom panel). The orange lines indicate the average bond length over the entire MD trajectory.

Table S1 Average bond lengths, standard deviations, and maximum deviations of the C-N, C-O, and C-C bonds in the SWCNT-M1-SWCNT junction shown in Figure S2 at 300 K and 500 K.

Bond type	C-N		C-O		C-C	
	300	500	300	500	300	500
Average bond length (Å)	1.37	1.37	1.37	1.37	1.42	1.42
Standard deviation (Å)	0.026	0.034	0.028	0.037	0.027	0.036
Maximum deviation (Å)	0.10	0.15	0.12	0.15	0.10	0.15
Bond length calculated using DFT (Å)	1.39		1.40		1.39	

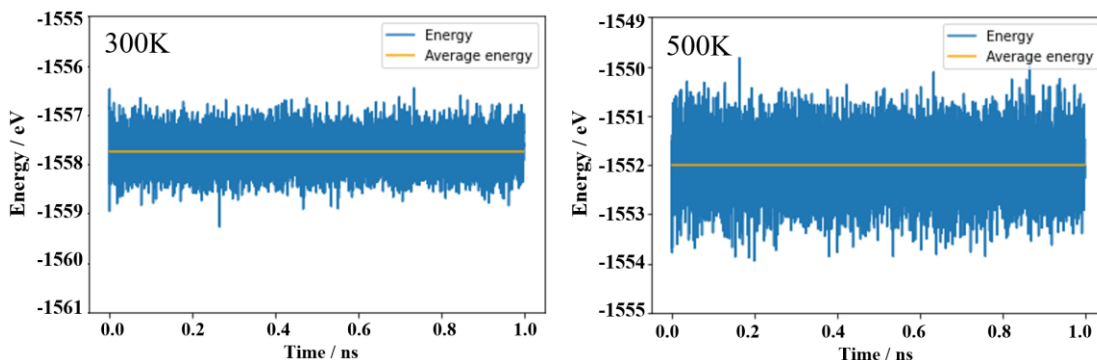


Figure S3 Variation in the total energy of the SWCNT-M1-SWCNT junction obtained from MD simulations performed at 300 K (the left panel) and 500 K (the right panel). The orange lines indicate the average energy over the entire MD trajectory.

Table S2 Average energies, standard deviations, and maximum deviations of the total energies of the SWCNT-M1-SWCNT junction shown in Figure S3 at 300 K and 500 K.

Temperature (K)	300	500
Average energy (eV)	-1557.74	-1552.00
Standard deviation (eV)	0.34	0.56
Maximum deviation (eV)	1.53	2.18

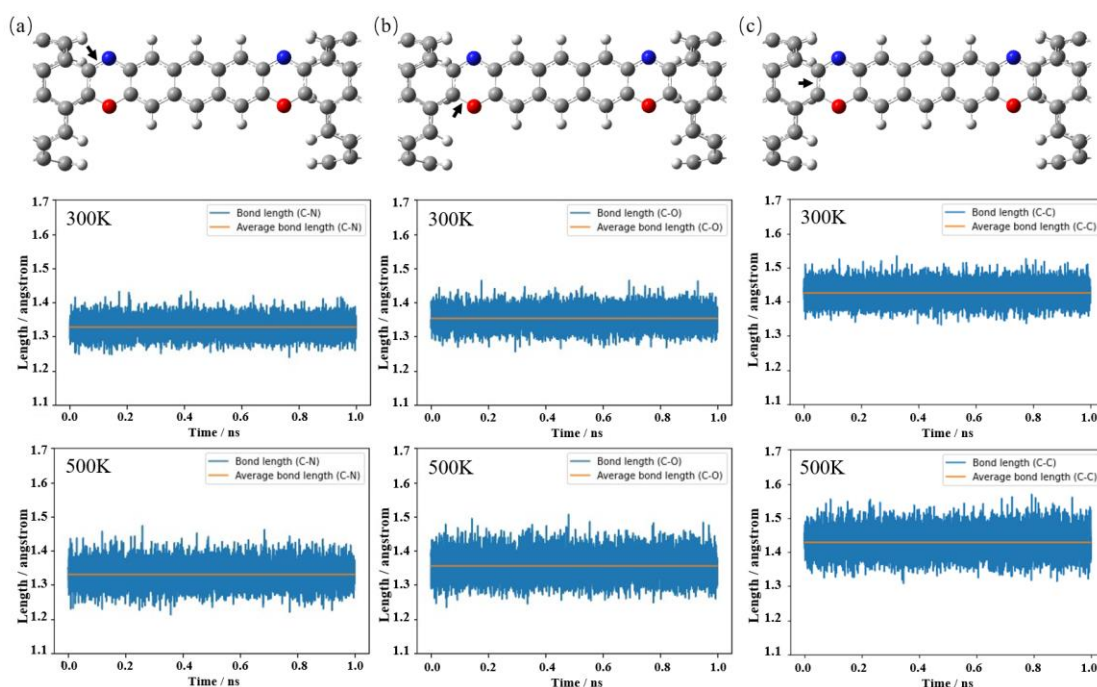


Figure S4 Variation in the C-N (a), C-O (b) and C-C (c) bond lengths marked by black arrows (the upper panel) in the SWCNT-M1^{dH}-SWCNT junction obtained from MD simulations performed at 300 K (the middle panel) and 500 K (the bottom panel). The orange lines indicate the average bond length over the entire MD trajectory.

Table S3 Average bond lengths, standard deviations, and maximum deviations of the C-N, C-O and C-C bonds in the SWCNT-M1^{dH}-SWCNT junction shown in Figure S4 at 300 K and 500 K.

Bond type	C-N		C-O		C-C	
	300	500	300	500	300	500
Temperature (K)	300	500	300	500	300	500
Average bond length (Å)	1.33	1.33	1.35	1.35	1.42	1.42
Standard deviation (Å)	0.025	0.032	0.027	0.36	0.027	0.036
Maximum deviation (Å)	0.11	0.14	0.11	0.15	0.11	0.14
Bond length calculated using DFT (Å)	1.35		1.38		1.43	

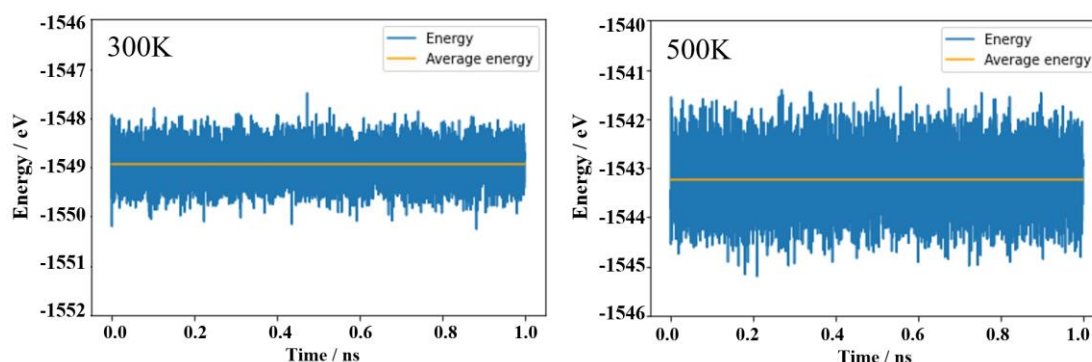


Figure S5 Variation in the total energy of the SWCNT-M1^{dH}-SWCNT junction obtained from MD simulations performed at 300 K (the left panel) and 500 K (the right panel). The orange lines indicate the average energy over the entire MD trajectory.

Table S4 Average energies, standard deviations, and maximum deviations of the total energies of the SWCNT-M1^{dH}-SWCNT junction shown in Figure S5 at 300 K and 500 K.

Temperature (K)	300	500
Average energy (eV)	-1548.94	-1543.24
Standard deviation (eV)	0.34	0.56
Maximum deviation (eV)	1.44	1.97

Molecular dynamics (MD) simulations are performed with the xtb program,² where forces and energies are calculated using the GFN-FF force field.³ The Newtonian equations of motion of the atoms in the junction are then integrated via the velocity Verlet algorithm with a time step of 1.0 fs. A Berendsen thermostat maintains the average temperature at either 300 K or 500 K. Along the MD trajectories the configurations are recorded every 100 fs.

At the selected temperatures we run MD calculations for the SWCNT-M1-SWCNT junction for 1ns, recording 10,000 configurations. The SWCNT-M1-SWCNT

junction is very stable at room temperature (300 K) and even when the temperature is increased to 500 K, we do not observe the occurrence of any bond cleavage. For the typical C-N, C-O and C-C bonds at the molecule-electrode interface, the average bond lengths, standard deviations, and maximum deviations are listed in Table S1. As we can see, the average bond lengths of the C-N, C-O and C-C bonds are respectively calculated to be 1.37, 1.37 and 1.42 Å, which are in good agreement with the DFT optimized values of 1.39, 1.40 and 1.39 Å. This further confirms the reliability of the GFN-FF force field for the material set investigated. At room temperature, the maximum deviations for these three bonds are 0.10~0.12 Å. When the temperature increases to 500 K, the maximum deviations are 0.15 Å, illustrating the robustness of these covalent bonds. Similar results are also obtained from MD simulations for the SWCNT-M1^{dH}-SWCNT junction, for which we also record 10,000 configurations along 1 ns and do not find any bond cleavage even at 500 K. As shown in Table S3, the average bond lengths of the C-N, C-O and C-C bonds are respectively calculated to be 1.33, 1.35 and 1.42 Å, which are also in excellent agreement with the DFT optimized values of 1.35, 1.38 and 1.43 Å. Considering the small standard deviations of both bond lengths and total energies (Tables S1-S4), we can conclude that the covalent oxazine anchors are advantageous for forming stable and robust molecular junctions with SWCNT electrodes.

Section 3: Frontier molecular orbitals of the M1 and M1^{dH} molecules in the gas phase

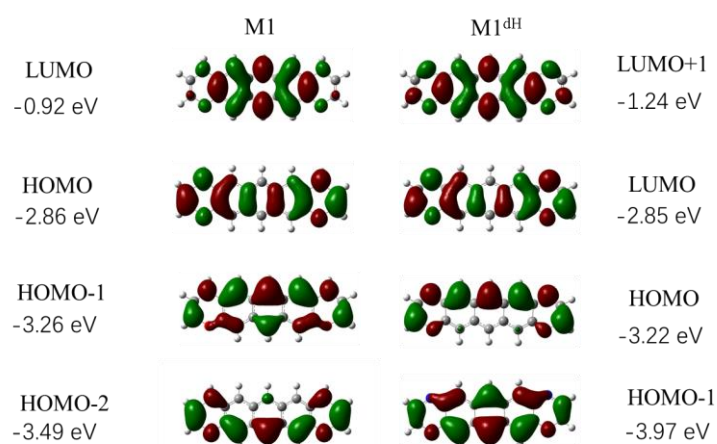


Figure S6 Frontier molecular orbitals (FMOs) of the isolated M1 and M1^{dH} molecules

Section 4: Comparison of typical bond lengths at the molecule-electrode interfaces in the graphene-M1-graphene and graphenen-M1^{dH}-graphene junctions

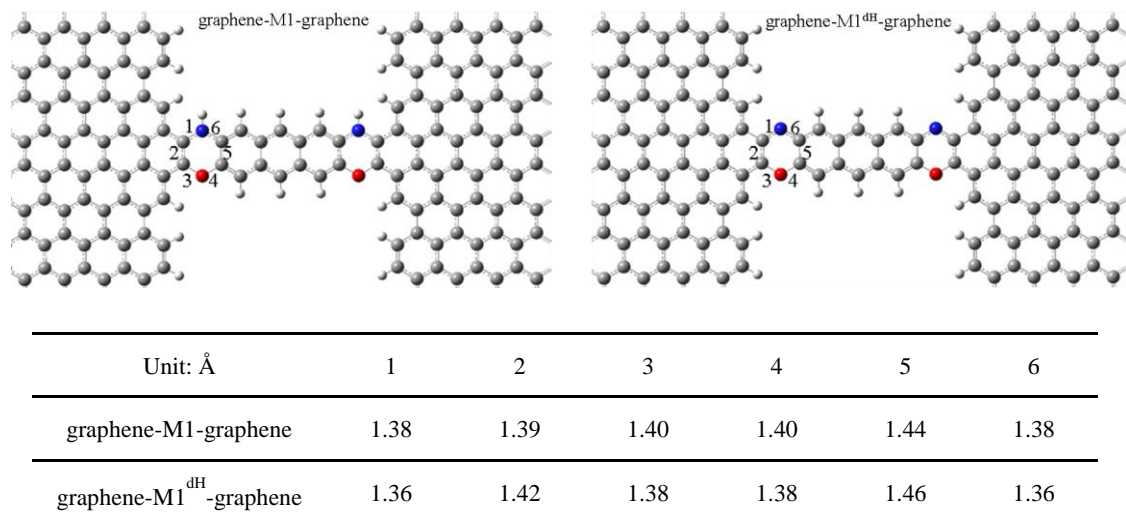


Figure S7 Typical bond lengths at the molecule-electrode interfaces of graphene-M1-graphene and graphene-M1^{dH}-graphene junctions

Section 5: Transmission plots with their vertical axes set to a logarithmic scale

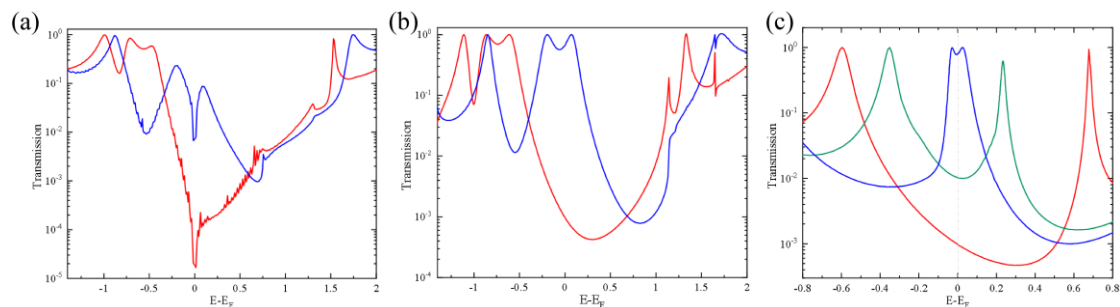


Figure S8 The transmission spectra of graphene-M1-graphene (red line) and graphene-M1^{dH}-graphene (blue line) in (a), and of SWCNT-M1-SWCNT (red line) and SWCNT-M1^{dH}-SWCNT (blue line) in (b), and of SWCNT-M21-SWCNT (red line), SWCNT-M22-SWCNT (green line) and SWCNT-M23-SWCNT (blue line) in (c).

It should be noted that the dip in the transmission spectra around the Fermi level of the graphene-M1-graphene and graphene-M1^{dH}-graphene junctions (see Figure S8a) originates from the electronic properties of the graphene electrodes. Since the DOS of

graphene approaches zero at the Fermi level, there are no electrons incident at this energy so that the transmission should be strictly zero. However, due to the finite k -points sampled in the the one-dimensional Brillouin zone orthogonal to the transport direction, a transmission dip with a finite depth is always present in numerical calculations.

Section 6: Optimized atomic structures and equilibrium transmission spectra of the junctions constructed with nitrogen-doped graphene electrodes

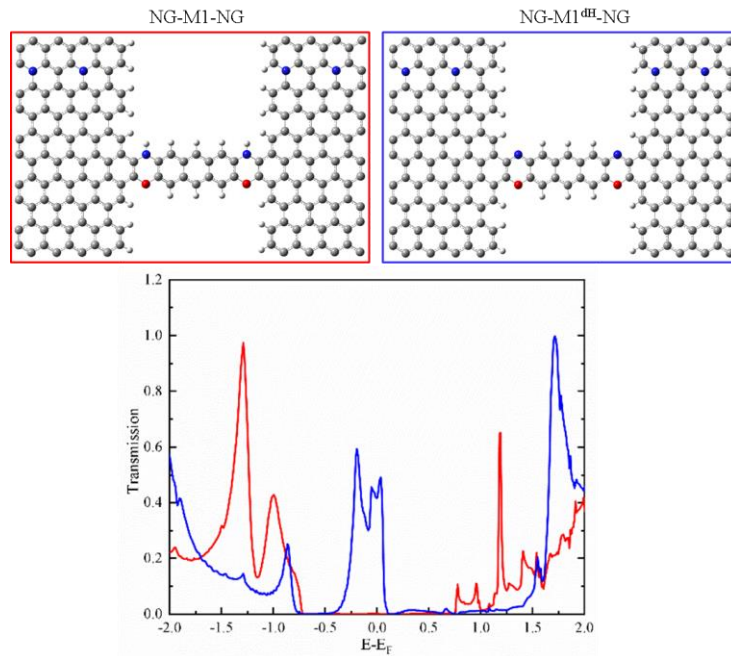


Figure S9 Optimized atomic structures as well as the corresponding transmission spectra of the NG-M1-NG (red line) and NG-M1^{dH}-NG (blue line) junctions. Here, NG denotes nitrogen-doped graphene.

Section 7: Optimized atomic structures and equilibrium transmission spectra of the junctions constructed with different SWCNT electrodes or molecule-electrode interfacial configurations

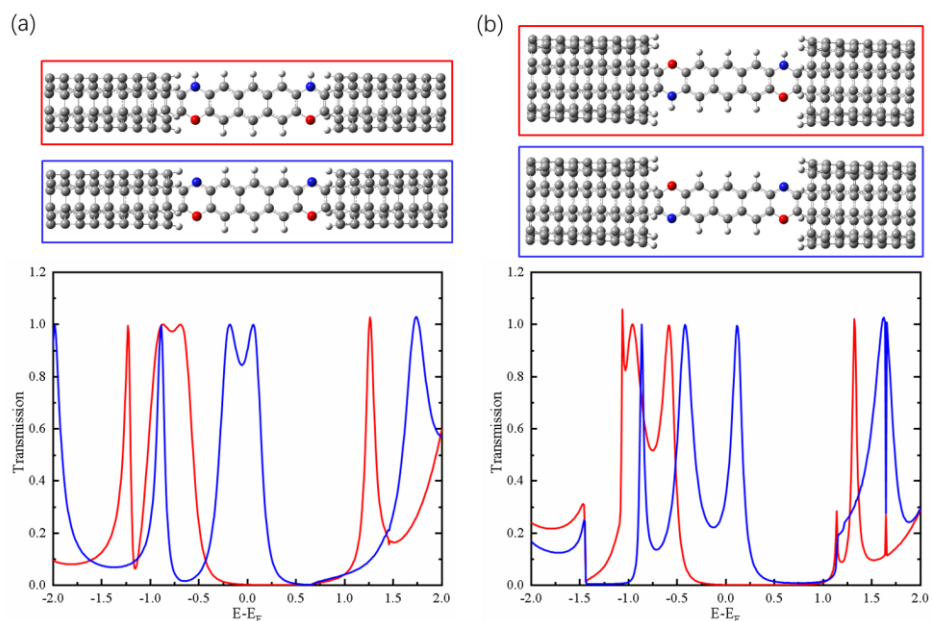


Figure S10 (a) Optimized atomic structures and the corresponding transmission spectra of molecule junctions in which M1/M1^{dH} is connected to two semi-infinite (3, 3) armchair SWCNT electrodes. (b) Optimized atomic structures and the corresponding transmission spectra of molecule junctions in which the symmetry of the two oxazine linkers is opposite to that of SWCNT-M1/M1^{dH}-SWCNT.

Section 8: Optimized atomic structures and equilibrium transmission spectra of the junctions with the molecular backbone modified by different functional groups

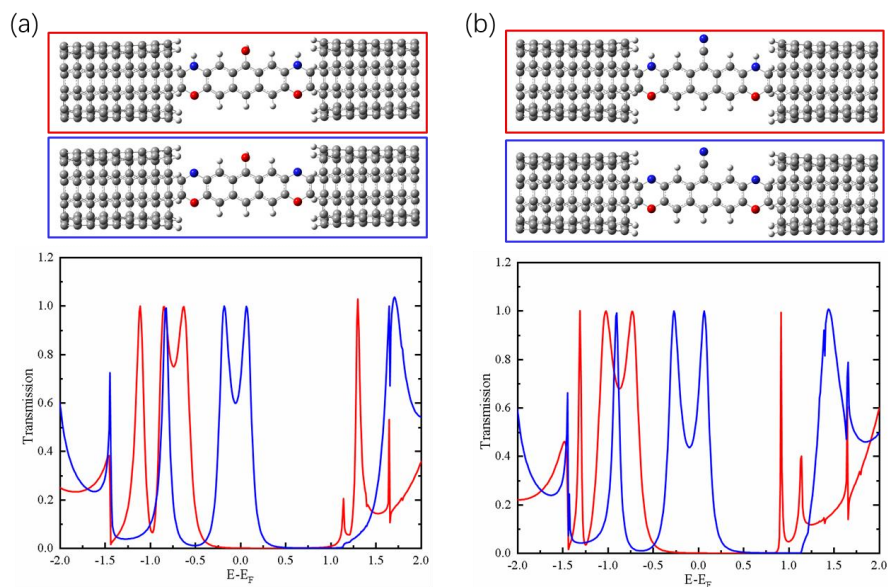


Figure S11 Optimized atomic structures and the corresponding transmission spectra of molecule junctions in which the central benzene ring in M1 is functionalized with an oxhydryl group (a) or a cyano group (b)

Section 9: Optimized atomic structures and equilibrium transmission spectra of the junctions constructed with different central molecules

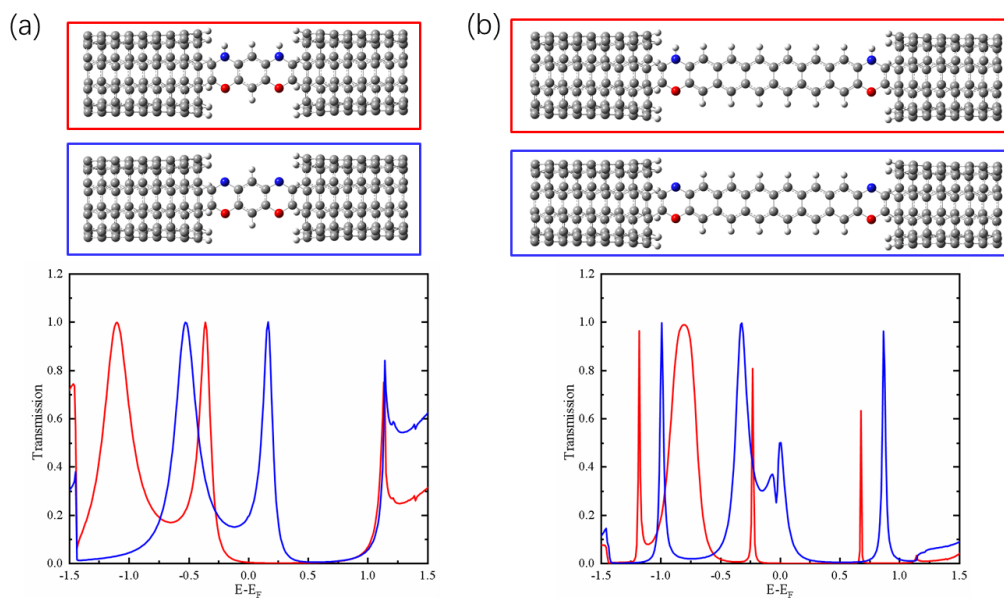


Figure S12 Optimized atomic structures and the corresponding transmission spectra of molecule junctions in which the anthracene molecule in the SWCNT-M1/M1^{dH}-SWCNT junction is altered to a benzene (a) or a hexacene (b) molecule

Section 10: Frontier molecular orbitals of the isolated M21, M22 and M23 molecules, together with the conducting eigenchannels for selected transmission peaks of the SWCNT-M21-SWCNT, SWCNT-M22-SWCNT and SWCNT-M23-SWCNT junctions around the Fermi level

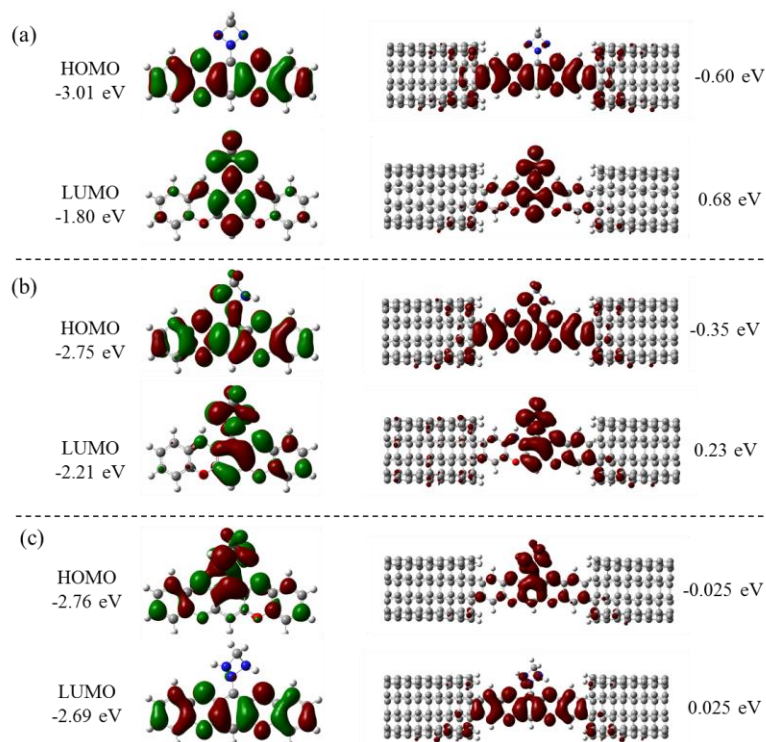


Figure S13 Frontier molecular orbitals of the isolated M21 (a), M22 (b), and M23 (c) molecules, together with the conducting eigenchannels for selected transmission peaks of the SWCNT-M21-SWCNT (a), SWCNT-M22-SWCNT (b), and SWCNT-M23-SWCNT (c) junctions around the Fermi level.

Section 11: Molecular orbital analysis for the isolated M21 and M23 molecules

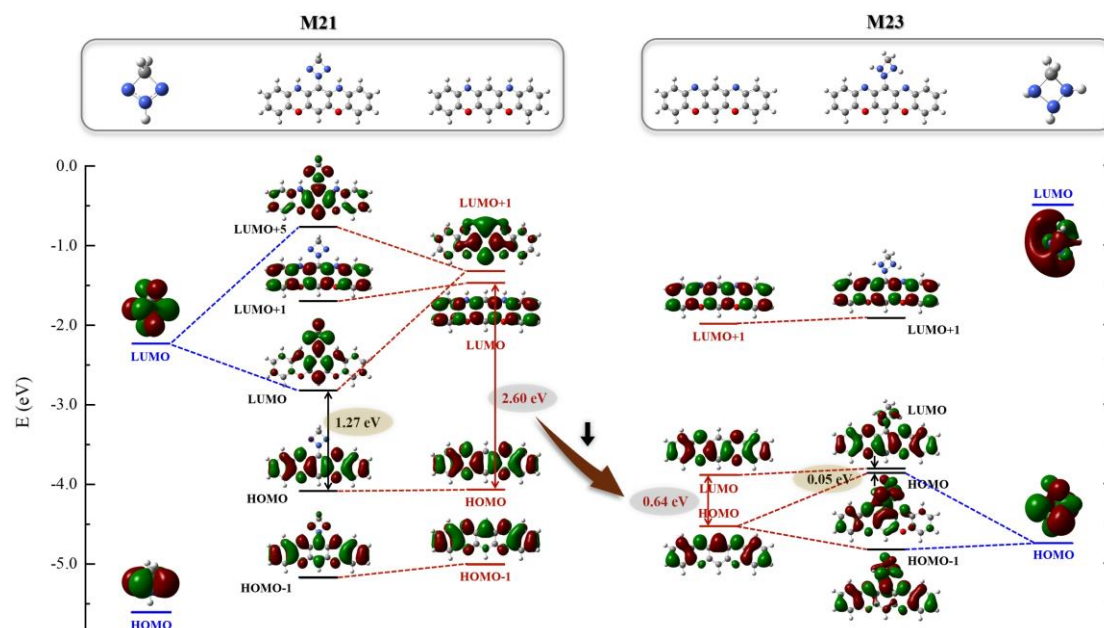


Figure S14 Molecular orbital energy level diagrams for the isolated M21 and M23 molecules calculated using the Gaussian16 package at the PBE/6-311+G(d, p) level

As shown in Figure S14, an isolated M21 molecule can be decomposed into two parts: the molecular bridge and the dehydrogenated triazetidine moiety. The π -type LUMO of the dehydrogenated triazetidine moiety couples strongly with the LUMO+1 orbital of the molecular bridge, forming respectively the LUMO and LUMO+5 orbitals of M21. This results in a much smaller HOMO-LUMO gap (1.27 eV) of M21, compared to that of the molecular bridge (2.60 eV). After two hydrogen atoms are transferred from the molecular bridge to the triazetidine moiety forming the M23 molecule, the HOMO-LUMO gap of the dehydrogenated molecular bridge is drastically reduced to 0.64 eV. Moreover, the coupling between the σ -type HOMO of the triazetidine moiety and the HOMO of the dehydrogenated molecular bridge pushes up in energy the HOMO of the M23 molecule, further reducing the M23 HOMO-LUMO gap to 0.05 eV. Therefore, the significantly diminished HOMO-LUMO gaps of M21-M23 upon intramolecular proton transfer originates from the synergistic effects of the molecular bridge and the triazetidine moiety.

Section 12: Effects of the applied electric field on the M22-to-M23 transformation

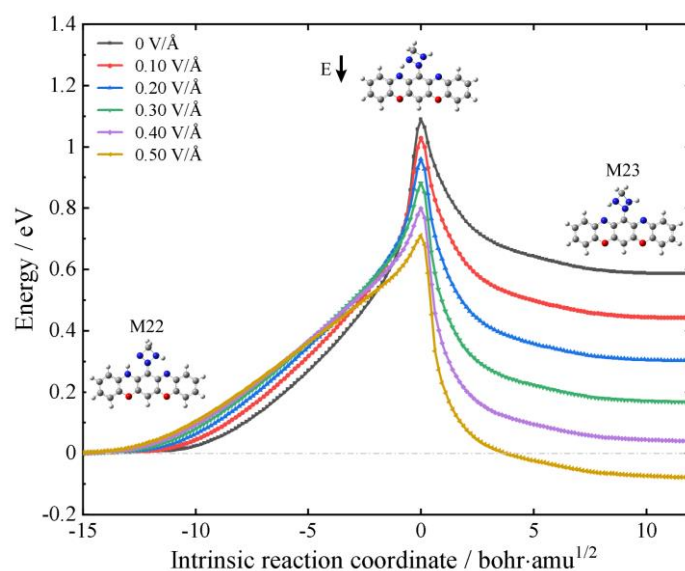


Figure S15 Energy along the intrinsic reaction path from M22 to M23 in the gas phase. An external electrostatic field (indicated by a black arrow in the inset) could control the relative stability of M22 and M23 as well as the energy barrier for their interconversion. Specifically, M23 becomes more stable than M22 at the field of 0.50 V/Å.

References:

- 1 T. Frederiksen, M. Paulsson, M. Brandbyge and A.-P. Jauho, *Phys. Rev. B*, 2007, **75**, 205413.
- 2 C. Bannwarth, E. Caldeweyher, S. Ehlert, A. Hansen, P. Pracht, J. Seibert, S. Spicher and S. Grimme, *WIREs Comput. Mol. Sci.*, 2021, **11**, e1493.
- 3 S. Spicher and S. Grimme, *Angew. Chem. Int. Ed.*, 2020, **59**, 15665-15673.